The oscillation of gas bubbles in tubes: Experimental results

X. Geng, H. Yuan, H. N. Oğuz, and A. Prosperetti[a)]
Department of Mechanical Engineering, The Johns Hopkins University, Baltimore, Maryland 21218

(Received 5 October 1997; accepted for publication 15 April 1999)

An experimental study is presented of the frequency dependence and damping of the forced volume oscillations of gas bubbles in liquid-filled tubes. The bubbles occupy the entire section of the tube and are driven by a needle attached to a loudspeaker cone. The liquids used were water, a water–surfactant solution, and silicon oil, and the tube diameters were 1 and 3 mm. The results are in excellent agreement with the theory developed in two earlier papers. This work is motivated by the possibility of using gas bubbles as actuators in fluid-handling microdevices. © *1999 Acoustical Society of America.* [S0001-4966(99)04807-9]

PACS numbers: 43.35.Pt, 43.20.Ks, 47.55.Dz [HEB]

INTRODUCTION

In two recent papers, a theory was presented for the natural frequency[1] and damping[2] of the oscillations of gas bubbles in liquid-filled tubes. In the present study, we describe an experimental investigation that is in excellent agreement with the theoretical predictions.

While an extensive literature exists on the small-amplitude volume oscillations of gas bubbles in unbounded liquids (reviewed, for instance, in Refs. 3–6), the physics of bubbles confined in channels and tubes presents such substantial differences that a specific investigation is necessary. This statement is especially applicable to the bubbles considered here, which are large enough to occupy an entire section of the tube. Indeed, in this case, the inertia of the system is entirely dependent on the length of the liquid columns on either side of the bubble, rather than being proportional to the bubble volume. Furthermore, the liquid flow in the tube can be strongly affected by viscosity which, for free bubbles, is usually unimportant except for very small radii.

This work is motivated by the possibility to use gas bubbles as actuators in the small fluid-handling systems that advances in silicon manufacturing technology render possible (see, e.g., Refs. 7–9). One of the attractive features of such an application is that gas bubbles can be powered remotely by ultrasonic sources with no need for direct contact between the actuator and the power supply.

I. EXPERIMENT

Glass tubes with a diameter of 1 and 3 mm were used with water, silicon oil, and a surfactant solution of 50 ppm Triton-X-100 in water. This amount is about 37% of the critical micellar concentration. A drop of liquid was placed in the desired position in the upper part of the tube by means of a hypodermic syringe. A second drop was introduced so as to fill the lower part of the tube, leaving an air gap between its upper surface and the lower surface of the first drop. A stainless-steel needle of suitable size, cut perpendicularly to the axis and plugged with silicon glue, was filed so as to fit snugly, and then inserted into the lower end of the tube leaving no air gap between its tip and the lower liquid region. The length of the liquid column separating the needle tip from the lower surface of the bubble was of the order of 10–20 mm. The needle was attached to a loudspeaker driven by an amplifier and function generator while the glass tube was mounted in a fixed plexiglass plate (Fig. 1).

The objective of the experiment was to determine the amplitude of oscillation of the gas volume as a function of frequency. For this purpose, a charge-coupled device (CCD) camera was used to take digital snapshots of the bubble at equally spaced time intervals. Since the speed of the camera was not sufficient to record the necessary number of pictures during a single cycle, pictures were taken at time intervals $nT+\Delta t$, with T the period of the needle oscillations, n a suitable integer (such that $nT \simeq 500$ ms), and $\Delta t = 0.1$ ms, which gives 30 to 100 frames per cycle depending on the driving frequency. Sample sequences of the pictures acquired in this way are shown in Figs. 2–5.

The digital images produced by the CCD camera were scanned to determine the position of the surface bounding the gas space. From this digitized version of the bubble surface, with the assumption of axial symmetry, the instantaneous bubble volume $V(t)$ could be computed. The image processing was carried out automatically in real time during

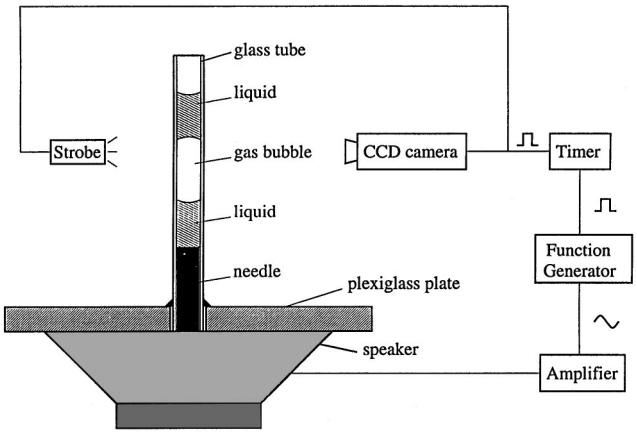

FIG. 1. Sketch of the experimental apparatus. The tube containing the two liquid columns separated by the air bubble is inserted onto a needle fastened to a loudspeaker cone. The loudspeaker is driven by a function generator connected through an amplifier.

[a)]Electronic mail: prosper@titan.me.jhu.edu

the course of the experiment, and there was no need to store the images.

The bubble volume was converted to an effective length L_e by

$$L_e(t) = V(t)/S, \tag{1}$$

where S is the tube cross-sectional area. Since we did not correct for refraction, the CCD images are distorted. However, by comparing the needle image when inside the liquid-filled tube and in air, we established that the distortion was a constant independent of the distance from the tube axis, much in the same way as the effect produced by a lens. Since S in Eq. (1) was also measured from the same images, the final value of L_e is therefore unaffected by the optical distortion. Before running the experiment, the initial value L_0 of the effective bubble length was measured in the same way.

For all frequencies, we took 200 data points and least-squares fitted them to an expression of the form

$$L(t) = A_B \cos(\omega t + \phi) + ct + L', \tag{2}$$

where ω is the angular frequency of the driver and A_B, ϕ, c, and L' are determined from the fit. The largest difference between the value of L' obtained from the fit and the initial value L_0 was about 1%. The term ct was included to account for any drift due, e.g., to loss of liquid leaking past the needle, but in all cases it was found to be very small, with a contribution of the order of 1% or less. After the determination of the parameters in (2), an error ϵ_B was computed from

$$\epsilon_B = \sqrt{\frac{1}{N-1}\sum_{k=1}^{N}[L(t_k) - L_e(t_k)]^2}, \tag{3}$$

with L calculated from (2) and L_e the measured data; the sum is over all the data points.

The same process was carried out to determine the oscillation amplitude A_N of the needle and the corresponding error ϵ_N. The total error ϵ affecting the normalized oscillation amplitude

$$Z = A_B/A_N, \tag{4}$$

was compounded quadratically

$$\epsilon = \frac{\sqrt{\epsilon_B^2 + Z^2\epsilon_N^2}}{A_N}. \tag{5}$$

This is the length of the error bars shown in the comparison of data and theory in the following figures.

We found that, if the absolute amplitude of the volume oscillations was too large, surface instabilities [see, e.g., the right surface of the bubble in frame 5 of Fig. 2(b)] tended to disrupt the bubble and to cause significant error in the data. Also at large amplitudes, sometimes the bubble surface loses its definition [see, e.g., the left surfaces in frame 4 of Fig. 2(a) and frames 4 and 5 of Fig. 2(b)] and the edge-detection algorithm fails. (This situation was only encountered in the 1-mm-diameter tube with water, which is the reason we also used the surfactant solution in this tube.) Similarly, when the drive was too weak, the quality of the data was also poor. For this reason, as the frequency was varied, the driving amplitude was continuously adjusted so as to avoid these two extreme conditions. To test for hysteresis effects, the experiment was run by starting the frequency sweeps both from below and above the resonance frequency of the bubble. The results were, however, the same with the two procedures.

II. THEORY

As in Ref. 2, the bubble is schematized as a cylinder the length of which varies in the course of the oscillations. It was shown in Ref. 1 that, as far as the effective ''mass'' and ''spring'' of the equivalent oscillator are concerned, this is an excellent approximation even for bubbles that do not quite occupy the entire cross section of the tube, provided the length of the liquid columns is not too small. As far as thermal effects are concerned, the neglect of the curvature of the liquid–gas interface has the effect of slightly underestimating the area available for heat transfer. This might by undesirable for very short bubbles, but not here, where most of the bubble surface area actually consists of the lateral tube surface. Thus, we believe the model to be applicable, which, as will be seen later, is confirmed by the comparison with the data.

The situation considered here exhibits minor differences with respect to that of Ref. 2, and it is therefore necessary to modify slightly the relations derived there.

Let $x(t)$ denote the position of the liquid column separating the bubble from the ambient, and $x_N(t)$ the position of the liquid column forced by the needle, both measured from the respective equilibrium positions. The instantaneous length of the bubble is

$$x(t) - x_N(t) = L_0[1 + X(t)], \tag{6}$$

where L_0 is the undisturbed initial length and $X(t)$ the dimensionless amplitude of oscillation. The pressure in the bubble can be assumed spatially uniform and is written as

$$p(t) = p_0[1 - \Phi X(t)], \tag{7}$$

where p_0 is the equilibrium (ambient) pressure and Φ a complex quantity, explicitly given in Ref. 2, dependent on the ratio γ of the gas specific heats and on the parameters

$$\mathcal{A} = 1 + \frac{L_0}{R}, \quad \Omega = \frac{\omega}{4D(1/L_0 + 1/R)^2}, \tag{8}$$

in which $\omega = 2\pi f$ is the angular frequency of the driver, R the radius of the tube, and D the gas thermal diffusivity. The real and imaginary parts of Φ are shown as functions of Ω in Fig. 12 for $\gamma = 1.4$ and for aspect ratios $\mathcal{A} = 6$ and 12, which are close to those occurring in the experiments.

Let l be the length of the liquid column above the bubble. The equation of motion of this liquid column is

$$m\ddot{x} = -2\beta_v\dot{x} - p_0 S\Phi X, \tag{9}$$

where $m = lS\rho$ (with ρ the liquid density) is the mass of the liquid, S the cross-sectional area of the tube, and β_v the viscous damping parameter specified below. Upon substituting (6), we then have

$$L_0 m\ddot{X} + 2\beta_v L_0\dot{X} + p_0 S\Phi X = -m\ddot{x}_N - 2\beta_v\dot{x}_N. \tag{10}$$

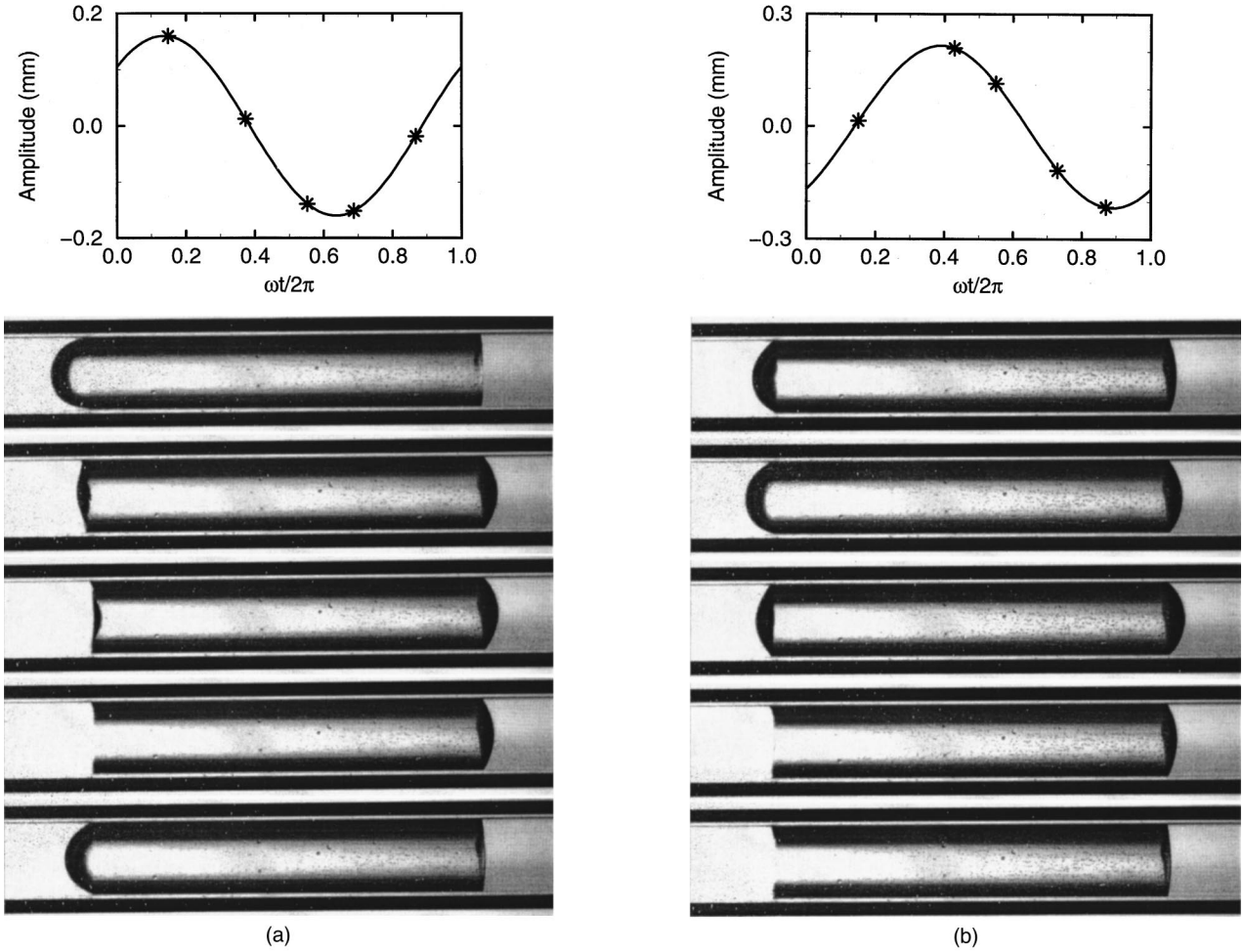

FIG. 2. Sample sequences of gas-bubble oscillations at 150 Hz (a) and 200 Hz (b) for pure water in the 1-mm-diameter tube. The bubble resonance frequency is 173 Hz. Other parameter values are given in Table I. The graphs above the photographic sequences show the position of each frame in the oscillation cycle. The data presented below are based on 200 such images. Time $t=0$ corresponds to the maximum upward displacement of the needle. Gravity acts from left to right. The needle is outside the frame to the right. The position of the contact line is clearly visible. Note the small drops on the glass surface, indicating that it is not covered by a liquid film. The bright bands along the sides of the tube are due to refraction in the glass.

The viscous damping parameter β_v is discussed in Ref. 2, where it is argued that it can be approximately calculated from

$$\beta_v = \frac{\nu m}{S}\left\langle \int_S \left[\frac{\partial}{\partial r}\left(\frac{u}{\dot{x}}\right)\right]^2 dS \right\rangle, \tag{11}$$

where ν is the liquid kinematic viscosity, the angle brackets denote the average over a cycle, the integration is over the cross section of the tube, r is the radial coordinate, and u is given by the solution of the Navier–Stokes equations for fully developed oscillatory flow (see, e.g., Ref. 10). The integral cannot be evaluated in closed form and it is graphed in Fig. 8 of Ref. 2. Asymptotic approximations are readily available for conditions in which the viscous penetration length, $\sqrt{\nu/\omega}$, is either much smaller or much larger than the tube radius R. In the former case (high frequency), dissipation occurs in a thin boundary layer and the result is

$$\beta_v = m\sqrt{\frac{\pi\nu\omega}{2S}}, \tag{12}$$

which is accurate for $R\sqrt{\omega/\nu}>30$, approximately. At low frequency ($R\sqrt{\omega/\nu}<3$), on the other hand, one finds

$$\beta_v = 4\frac{\nu m}{R^2}, \tag{13}$$

in agreement with the result for Poiseuille flow.

It should be noted that viscosity is not the only dissipative mechanism affecting the oscillations. The phase lag between the volume pulsations and the temperature oscillations in the gas causes a thermal damping that enters Eq. (10) through the imaginary part of Φ. As will be seen in the next section, this contribution to the damping can be far more significant than the viscous one.

For steady sinusoidal forcing $x_N = A_N \exp i\omega t$, Eq. (10) is readily solved. The dimensionless oscillation amplitude Z defined in (4) is found to be

$$Z = \frac{L_0 m(\omega^2 - 2i\beta_v\omega)}{p_0 S\Phi + 2iL_0\beta_v\omega - L_0 m\omega^2}. \tag{14}$$

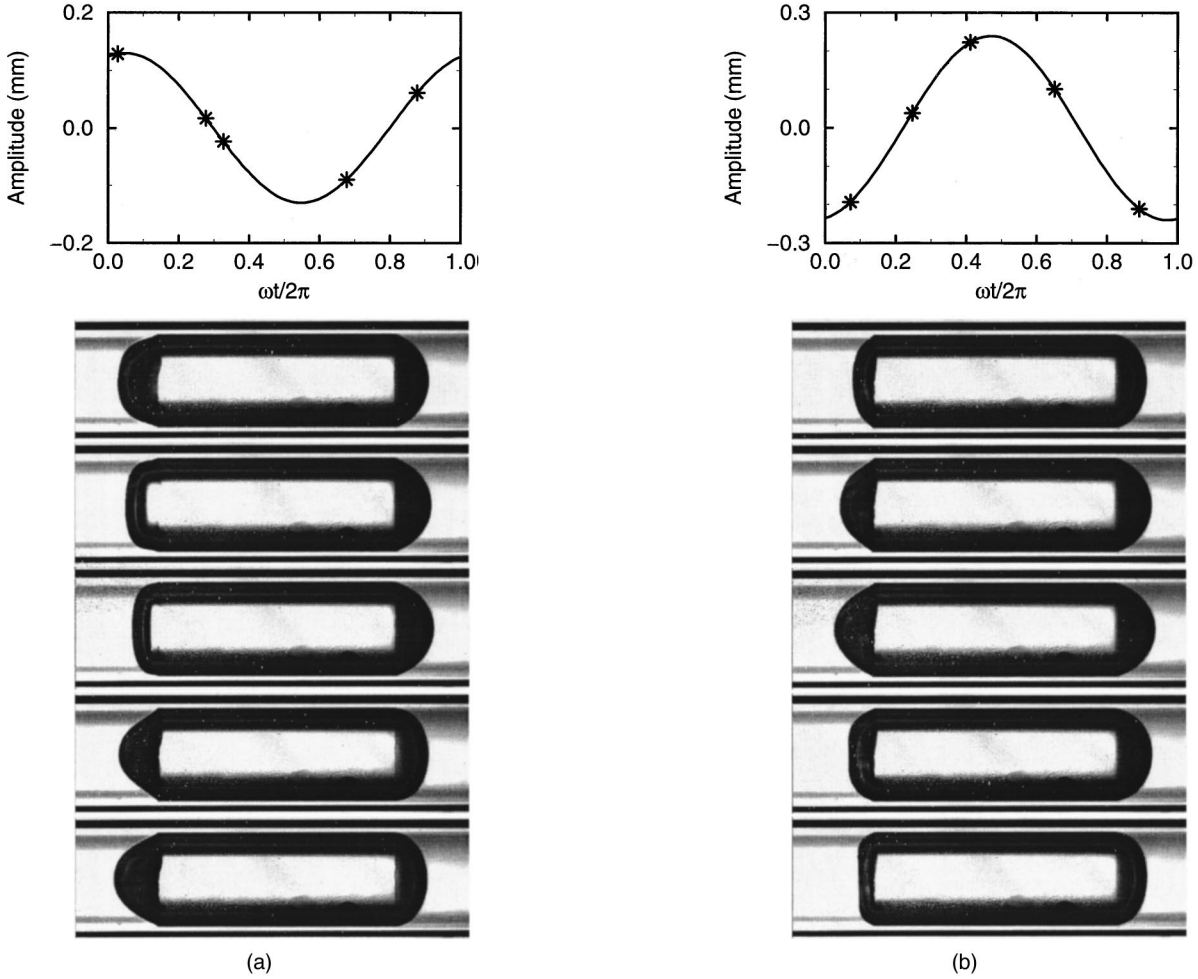

FIG. 3. Sample sequences of gas-bubble oscillations at 100 Hz (a) and 150 Hz (b) for pure water in the 3-mm-diameter tube. The bubble resonance frequency is 124 Hz. Other parameter values are given in Table I. The graphs above the photographic sequences show the position of each frame in the oscillation cycle. Time $t=0$ corresponds to the maximum upward displacement of the needle. Gravity acts from left to right. The needle is outside the frame to the right. The position of the contact line is clearly visible. Note the capillary waves on the left (upper) surface of the bubble.

III. RESULTS

Typical sequences of the pictures on which our data are based are shown in Figs. 2–5. The needle is on the right outside the field of view and the graph above each photographic sequence shows the position of each frame in the oscillation cycle. In these graphs, $t=0$ corresponds to the maximum upward displacement of the needle.

In interpreting these images, it should be kept in mind that the white stripes along the cylindrical body of the bubbles are not a residual liquid film, but an artifact due to refraction in the glass. The lateral boundary of the bubbles always appears to be the inner surface of the tube. For the case of water, this fact is confirmed by the tiny liquid drops visible in Figs. 2 and 3 on the tube surface. In some images of the water cases (Figs. 2, 3, and 4) the liquid–glass contact line is quite evident. The situation is not as clear for the silicon oil case of Fig. 5. As a matter of fact, we were unable to take data with silicon oil in the larger tube, because a thin liquid film was observed to flow from the upper to the lower bubble surface along the tube wall. The effect, if present at all, was much smaller for the 1-mm-diameter tube shown in Fig. 5 as no difference between the length of the liquid column above the bubble before and after the experiment could be measured.

In the pictures of Fig. 2 one can observe a very slight movement of the contact line. The effect is due to an excitation amplitude larger than that normally used to take data so as to illustrate more clearly the oscillation cycle. In all the other experiments, the amplitude of oscillation was small enough that the (dynamic) advancing and receding contact angles were not exceeded and the contact line was not observed to move.

Figures 2(a) and (b) have been taken with water in the 1-mm-diameter tube, below and above the resonance frequency of the bubble, respectively. This circumstance is evident from the fact that the liquid surfaces in Fig. 2(a) move in phase, while they have opposite phase in Fig. 2(b). A similar pattern is visible in Fig. 3 taken in the 3-mm-diameter tube. Several frames of Fig. 3 show evidence of the appearance of capillary waves on the bubble upper surface (on the left of the pictures). These waves are probably the result of a Faraday-type parametric amplification mechanism.

A striking qualitative difference between the two water

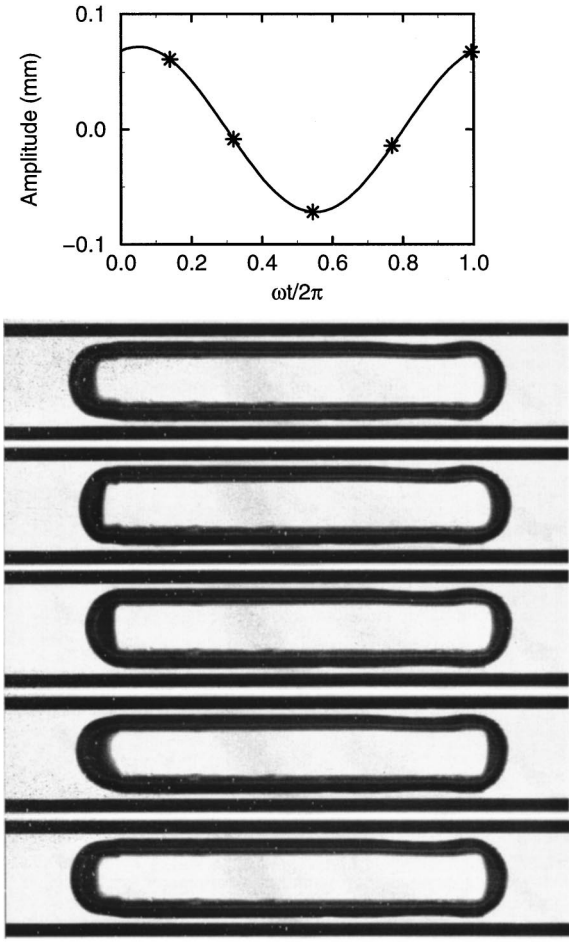

FIG. 4. Sample sequences of gas-bubble oscillations at 150 Hz for the water–Triton-X-100 solution in the 1-mm-diameter tube. The bubble resonance frequency is 189 Hz. Other parameter values are given in Table I. The graphs above the photographic sequences show the position of each frame in the oscillation cycle. Time $t=0$ corresponds to the maximum upward displacement of the needle. Gravity acts from left to right. The needle is outside the frame to the right. The position of the upper contact line is clearly visible on the left in frames 1, 2 , and 5. The slight curvature on the tube wall (upper right in the picture) is an optical artifact from an imperfection of the glass tube.

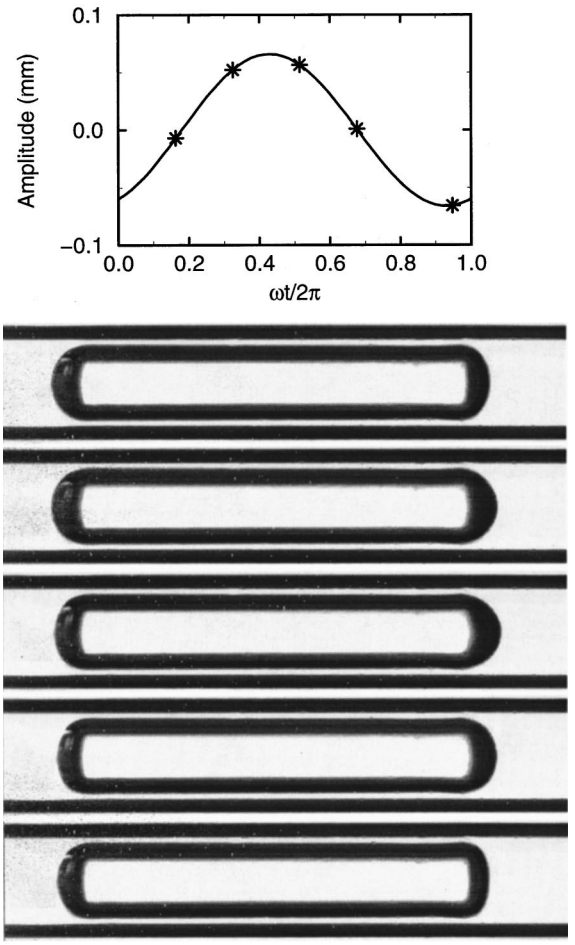

FIG. 5. Sample sequences of gas-bubble oscillations at 180 Hz for silicon oil in the 1-mm-diameter tube. The bubble resonance frequency is 235 Hz. Other parameter values are given in Table I. The graphs above the photographic sequences show the position of each frame in the oscillation cycle.

cases (Figs. 2 and 3) and the water–Triton and silicon ones (Figs. 4 and 5) is that, on average, the surface curvature seems to be much larger for the latter. This feature is a consequence of the difference in advancing and receding contact angles between the two systems. To illustrate the point, for pure water and the surfactant solution in the 1 mm-diameter tube, we show in Figs. 6 and 7 pairs of images: the upper one shows the bubble pushed into the tube by insertion of the needle, and the bottom one the equilibrium bubble shape before the sound is turned on. It is seen here, e.g., that the receding contact angle (at the top of the bubble, i.e., on the left of the images) is much larger for pure water than for the solution. It is therefore clear that, when the bubble stops (lower image in each pair), the pure water is much less curved than the Triton–water one. These static bubble shapes are essentially the average interface shape around which the bubble oscillates, and explain therefore the qualitative difference between the curvatures observed in Figs. 2, 4, and 5. Another interesting remark to be made, especially in connection with Fig. 6, is the strong difference between the (apparent) contact angles at the leading and trailing edges of the bubble. This is graphic evidence of the prevalence of a strong contact-angle hysteresis, which explains why the contact line does not move in the course of the oscillations.

Typical experimental results for the normalized oscillation amplitudes are compared with theory in Figs. 8 and 9

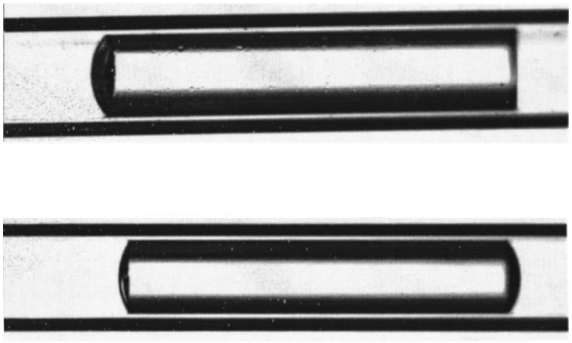

FIG. 6. The upper frame shows an air bubble as it is being pushed by the needle into the 1-mm-tube for pure water. The lower image is the same bubble at equilibrium. Note the marked difference between the advancing and receding contact angles in the upper image.

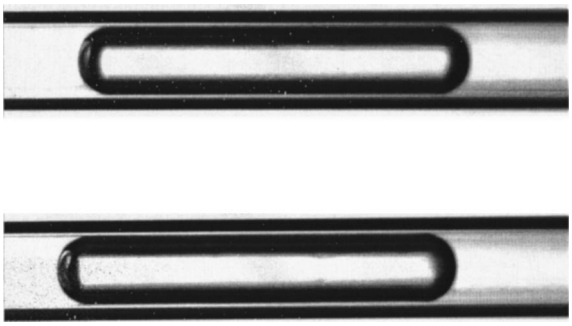

FIG. 7. The upper frame shows an air bubble as it is being pushed by the needle into the 1-mm-tube for the water–triton solution. The lower image is the same bubble at equilibrium. The difference between the advancing and receding contact angles is less in this case, but they are both smaller than in the pure-water case of the previous figure.

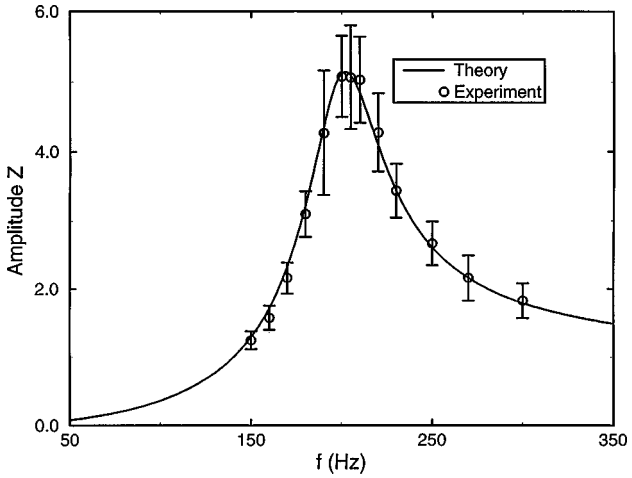

FIG. 8. Comparison between theory (solid line) and experiment for pure water in the 1-mm-tube. The normalized amplitude Z is defined in (4).

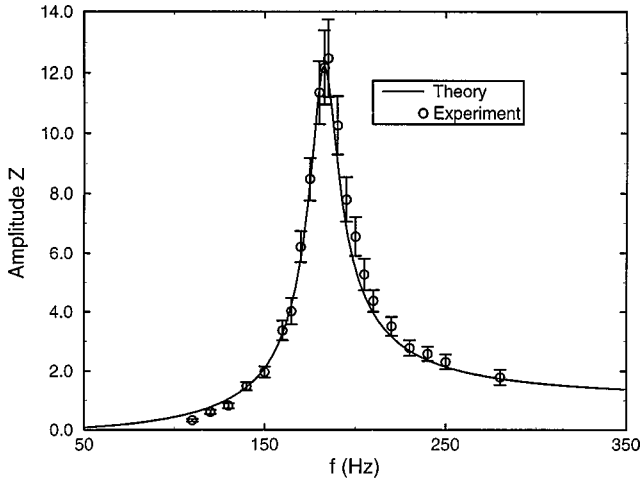

FIG. 9. Comparison between theory (solid line) and experiment for pure water in the 3-mm-tube. The normalized amplitude Z is defined in (4).

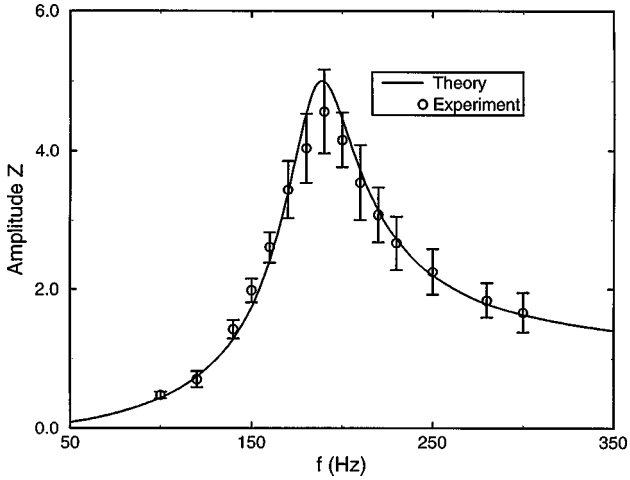

FIG. 10. Comparison between theory (solid line) and experiment for the water–Triton-X solution in the 1-mm-tube. The normalized amplitude Z is defined in (4). Note that, in contrast to the previous two cases, the maximum falls below the theoretical prediction, indicating the presence of additional dissipation due to surface effects not included in the theory.

(water), 10 (Triton-X-100 solution), and 11 (silicon oil). The relevant parameter values are given in Table I. It may be observed here that the experiments cover a range of the dimensionless frequency Ω where thermal effects in the bubble are significant, as can be seen from Fig. 12. Furthermore, while the high- and low-frequency approximations (12) and (13) are applicable to the 3-mm-diameter tube and the silicon oil cases, the range of dimensionless viscous penetration lengths for water and the surfactant solution in the 1-mm-diameter tube falls outside the limits of validity of the approximations, and the complete expression must be used. Thus, we feel that the present experiments constitute a meaningful test of the theory.

The two water cases of Figs. 8 and 9 display an excellent agreement with theory. Data acquisition is easier for the larger tube (Fig. 9), which accordingly has smaller error bars.

A very simplified theory of the phenomenon under consideration can be formulated neglecting thermal effects altogether and assuming an isothermal or adiabatic behavior of the gas. We show in Fig. 13 a comparison between the exact

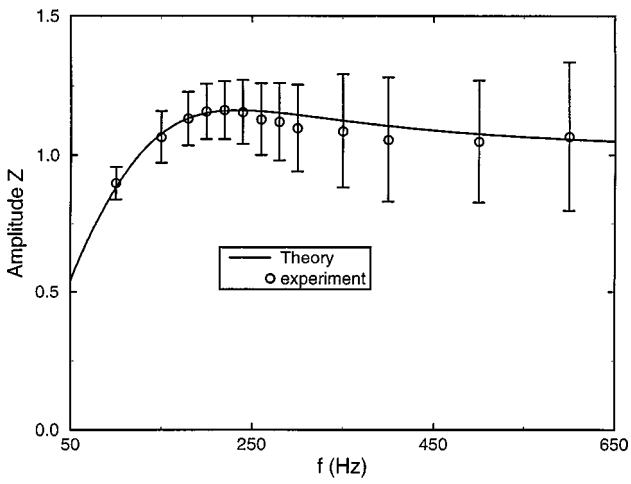

FIG. 11. Comparison between theory (solid line) and experiment for the silicon oil in the 1-mm-tube. The normalized amplitude Z is defined in (4).

TABLE I. Parameter values for the cases illustrated in the figures; l is the length of the upper liquid column, L_0 the undisturbed bubble length, and the dimensionless frequency Ω is defined in (8).

Figure no.	l (mm)	L_0 (mm)	$\mathcal{A}$	Res. freq. (Hz)	$\Omega_{\min}$	$\Omega_{\max}$	$R\sqrt{\omega_{\min}/\nu}$	$R\sqrt{\omega_{\max}/\nu}$
2(a),(b)	16.5	6.30	13.6	173	⋯	⋯	⋯	⋯
3(a),(b)	20.0	11.0	8.33	124	⋯	⋯	⋯	⋯
9	14.7	5.23	11.5	202	0.74	4.4	8.86	21.7
10	14.5	7.0	5.67	183	5.4	32.4	26.6	65.1
4, 11	15.0	5.85	12.7	189	0.75	4.5	8.86	21.7
5, 12	22.0	5.85	12.7	235	0.75	4.5	1.25	3.07

theory of Sec. II with three versions of a simplified theory for the case of Fig. 9. The solid line is the same as that shown in Fig. 9 and represents the complete theory. The dotted and dot-and-dash lines show the results obtained by neglecting thermal dissipation and assuming the gas to behave isothermally or adiabatically, respectively. The dashed line neglects thermal dissipation, but includes thermal effects in the calculation of the gas stiffness. It can be seen here that thermal effects play a substantial role not only in limiting the peak response through their effect on dissipation, but also in determining the gas stiffness and therefore the position of the resonance frequency.

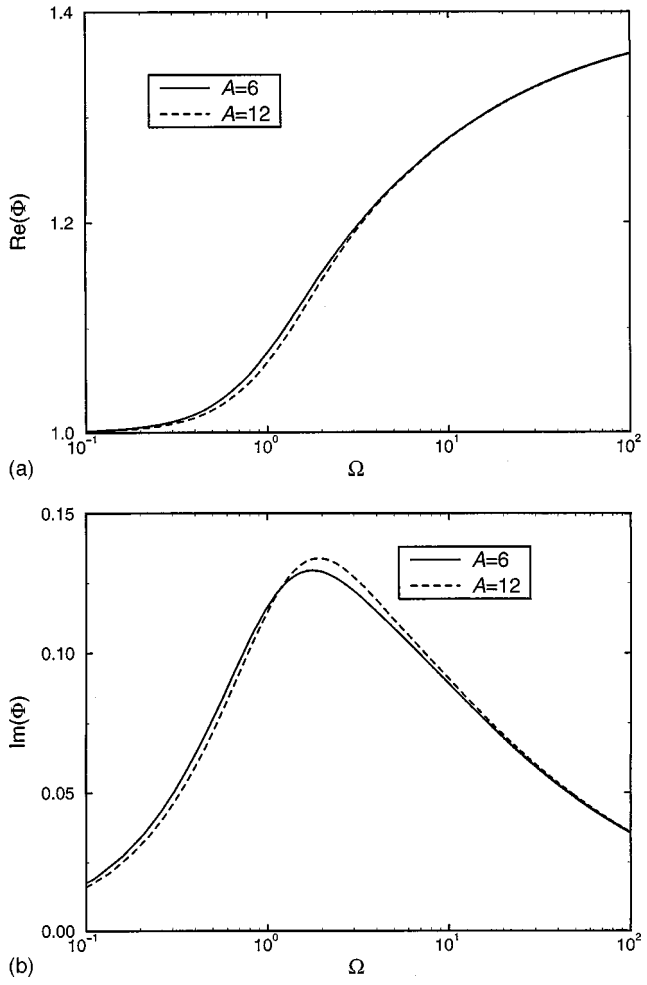

FIG. 12. Graph of the real (a) and imaginary (b) parts of the function Φ defined in Eq. (27) of Ref. 2 for $\gamma=1.4$ and aspect ratios $\mathcal{A}=6$ (solid) and 12 (dashed). The dimensionless frequency Ω is defined in (8).

Figure 10 is for the 50-ppm Triton-X-100 solution. In plotting the theoretical result, no account was taken of the presence of the surfactant and the same theory as for water was used. It is seen that, while this theory agrees with the data away from resonance, it overpredicts the resonant response. If one tries to fit the data by adjusting the liquid viscosity, a viscosity value about 40% greater than that of water would be necessary. This is completely unrealistic for the small concentrations used in the experiment. The Marangoni stresses set up by the inability of the surfactant concentration to follow the surface motion[11] at these relatively high frequencies are probably responsible for the additional dissipation encountered here. A more detailed investigation of this phenomenon falls outside the scope of the present study.

The bubble response in the highly viscous silicon oil is much smaller than in the water cases. The error bars appear therefore bigger, although in relative terms, around the maximum, they are comparable to those in the other figures. It may be observed that the model captures correctly the marked change of behavior between the low- and high-viscosity cases.

IV. CONCLUSIONS

In the present paper, we have compared experimental results for the forced oscillations of gas bubbles in tubes with

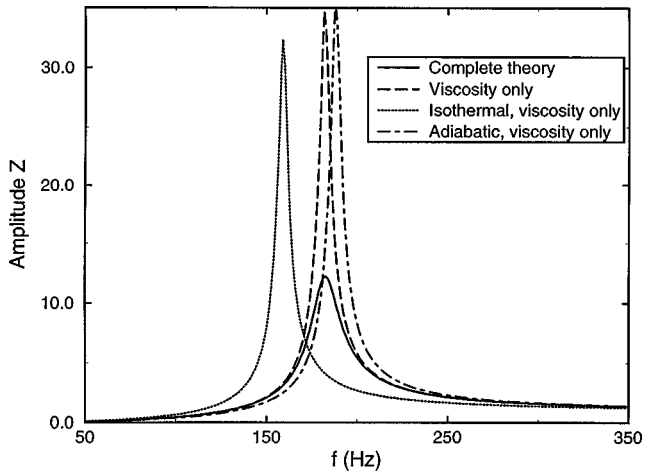

FIG. 13. Normalized oscillation amplitude as predicted by several theories. The solid line is the same one as shown in Fig. 9 and is the prediction of the complete theory. The dotted and dot-and-dash lines show the results obtained by neglecting thermal dissipation and assuming the gas to behave isothermally or adiabatically, respectively. The dashed line includes thermal effects in the calculation of the bubble stiffness, but neglects their contribution to energy dissipation.

a theory developed in two earlier studies. An excellent agreement has been found which, among other features, illustrates the importance of thermal phenomena in determining the bubble response.

An interesting side observation that can be made from the photographs taken in the course of the experiment is the graphic illustration of contact-angle hysteresis and its role in determining the equilibrium bubble shape and the lack of motion of the gas–liquid–glass contact line.

ACKNOWLEDGMENTS

We are grateful to Professor Kathleen Stebe for some useful comments. This study has been supported by AFOSR under Grant No. F49620-96-1-0386.

[1] H. N. Oğuz and A. Prosperetti, ''The natural frequency of oscillation of gas bubbles in tubes,'' J. Acoust. Soc. Am. **103**, 3301–3308 (1998).
[2] X. M. Chen and A. Prosperetti, ''Thermal processes in the oscillations of gas bubbles in tubes,'' J. Acoust. Soc. Am. **104**, 1389–1398 (1998).
[3] M. S. Plesset and A. Prosperetti, ''Bubble dynamics and cavitation,'' Annu. Rev. Fluid Mech. **9**, 145–185 (1977).
[4] R. E. Apfel, ''Acoustic cavitation,'' *Methods of Experimental Physics—Vol. 19 Ultrasonics*, edited by P. D. Edmonds (Academic, New York, 1981), pp. 355–411.
[5] A. Prosperetti, ''Bubble phenomena in sound fields: Part one,'' Ultrasonics **22**, 69–77 (1984).
[6] A. Prosperetti, ''Bubble phenomena in sound fields: Part two,'' Ultrasonics **22**, 115–124 (1984).
[7] H. Fujita and K. J. Gabriel, ''New opportunities for micro actuators,'' in *Transducers '91* (I.E.E.E., New York, 1991), pp. 14–20.
[8] L. Lin, A. P. Pisano, and A. P. Lee, ''Microbubble powered actuator,'' in *Transducers '91* (I.E.E.E., New York, 1991), pp. 1041–1044.
[9] P. Gravesen, J. Branebjerg, and O. S. Jensen, ''Microfluidics-a review,'' J. Micromech. Microeng. **3**, 168–182 (1993).
[10] L. G. Leal, *Laminar Flow and Convective Transport Processes* (Butterworth-Heinemann, Boston, 1992).
[11] C. D. Eggleton and K. J. Stebe, ''An adsorption–desorption controlled surfactant on a deforming droplet,'' J. Colloid Interface Sci. **208**, 68–80 (1998).